On the Bispectral Method for Cloud Parameter Determination from Satellite VISSR Data: Separating Broken Cloud and Semitransparent Cloud

C. M. R. PLATT

CSIRO Division of Atmospheric Physics, Aspendale, Victoria, Australia

(Manuscript received 27 October 1982, in final form 3 January 1983)

ABSTRACT

Using a physical model, bispectral curves of visible albedo versus infrared brightness temperature are derived for various idealized cloud layers. These layers vary between those which are unbroken with variable optical depth (cirrus) to those which are broken, but the clouds have a uniform high optical depth (stratocumulus). It is shown that the above two cases can be distinguished by the different shapes of the bispectral curves. The effects of variable solar angle and satellite viewing angle on the shapes of the bispectral curves are investigated. The effects of infrared scattering and deep cloud layers are also investigated and found to be important for high clouds with variable optical depth, such as cirrus.

The predicted curves are compared with two-dimensional bispectral histograms obtained from the VISSR radiometer of the GMS-1 satellite. The theoretical curves compare quite well qualitatively. Two detailed quantitative comparisons for clouds which are assumed to be semitransparent high clouds give good agreement.

The limitatins of the model are discussed.

1. Introduction

The International Satellite Cloud Climatology Programme (ISCCP) aims to obtain global cloud parameters over a five-year period, chiefly from satellite data. The required quantities for the ISCCP are fractional cloud cover, cloud top height, optical depth and cloud base height.

Although it is intended to use polar orbiting satellites to cover the polar regions and also possibly to identify areas of high cloud cover, the majority of the data will probably come from the visible (0.5–0.7 μm) and infrared (10–12 μm) scanning radiometers aboard five geosynchronous satellites situated strategically around the globe. It is thus vital to obtain optimum information from these two channels. Several techniques have recently been developed for this purpose, varying from simple threshold techniques and one-dimensinal histograms to the spatial coherence (Coakley and Bretherton, 1982) and bispectral techniques (Reynolds and Vonder Haar, 1977). It is the latter technique which is addressed in this article.

There are two different, but connected, aspects of the bispectral technique. First, the technique allows the calculation, with certain assumptions about cloud properties, of both fractional cloud amount and cloud optical depth as shown in the pioneering work of Reynolds and Vonder Haar (1977). Second, the relationships between cloud amount, albedo and emittance which are needed to solve the above parameters can be plotted in bispectral form to give patterns from which different cloud types can be visually identified.

The final aim of the technique in terms of the ISCCP is of course to recover the requisite parameters numerically from a specified set of equations. However, in the present developmental stage it is very useful to compare actual cloud data with predicted bispectral curves, to see whether the curves or patterns are unique for various cloud types and whether actual satellite data can be reconciled with the predicted curves.

In this article the bispectral curves for various idealized cloud layers, or combinations of cloud layers, will be presented. Since the early work of Reynolds and Vonder Haar, theoretical studies of scattering from clouds (for instance, Hansen, 1969; Liou, 1973; Stephens, 1978) have been compared with the data from observational studies (Stephens *et al.*, 1978; Platt *et al.*, 1980; Paltridge and Platt, 1981) to give a better understanding of the relationships between visible albedo, visible and infrared optical depth and infrared emittance. Although there are still some uncertainties, particularly regarding the albedo of ice clouds (Stephens, 1980), it is now possible to predict the bispectral properties of idealized cloud layers with some confidence.

As well as showing the typical curves for differences in cloud amount and optical depth and for both single and double cloud layers, the effects on these curves of variable solar zenith angle and satellite viewing angle are also considered. Some discussion is also given on the effects of infrared scattering and deep cloud layers.

Finally, the theoretical curves are compared with some observational data plotted in the form of bispectral two-dimensional histograms. Some remarks are also given on the relation to the infrared spatial coherence method of Coakley and Bretherton (1982), and to how the two methods might be combined.

2. Bispectral curves

a. Single layer

The scanning radiometers employed by the Geostationary Satellites scan sequentially across the earth's disc. Their resolution at the earth's surface is typically 1–2 km in the visible case and 5 km in the infrared case. The radiance recorded at the satellite is thus a measure of the integrated radiance within the radiometer field of view (FOV).

The data from the GMS-1 Japanese Geostationary Satellite is calibrated and transmitted in terms of a brightness temperature (T_e) in the infrared channel and an albedo (α_e) in the visible channel.

In this article, the dependencies of α_e and T_e on cloud amount and cloud optical depth δ (or IR emittance ϵ) are considered. To simplify the problem, and to investigate the broad characteristics of the above dependencies, an idealized single layer cloud is considered first. The cloud optical depth δ is allowed to vary from one field of view to the next, but is considered to be uniform within a single field of view. The fractional cloud cover is allowed to vary from one field of view to the next, but the cloud tops and heights remain constant, and the cloudy areas within the field of view are homogeneous and isothermal. The cloud is considered to scatter the incident solar radiation isotropically and the effects of scattering of infrared radiation on the radiances are neglected. The surface, which is viewed through gaps in the cloud, is assumed to be homogeneous and isotropic, to have an albedo typical of a sea surface, and to have an infrared emittance equal to unity.

Let the visible radiance at the satellite for a given FOV be $N_v(\theta, \phi, \xi)$, where θ is the solar angle of incidence at the cloud, ϕ the azimuth between the solar and satellite directions and ξ the nadir angle of the cloud at the satellite. For an isotropically reflecting cloud, the radiance is constant with ξ and ϕ. The radiance $N_v(\theta)$ can then be written

$$N_v(\theta) = F_0\pi^{-1}\left[m\alpha(\theta) + \frac{(1 - m\alpha')^2\alpha_g}{1 - \alpha'\alpha_g}\right], \quad (1)$$

where F_0 is the incoming solar flux, m is the fractional cloud amount, $\alpha(\theta)$ the albedo of the cloud to direct solar radiation, α' the diffuse albedo and α_g the albedo of the surface. The effects of Rayleigh scattering are neglected. The derivation of Eq. (1) includes multiple (diffuse) reflections between the cloud and the surface.

The corresponding albedo, obtained from a calibration is given by

$$\alpha_e = \pi N_v(\theta)F_0^{-1} = m\alpha(\theta) + \frac{(1 - m\alpha')^2\alpha_g}{1 - \alpha'\alpha_g}. \quad (2)$$

The radiances and albedos all refer to the bispectral range of the radiometer filter (0.5–0.7 μm wavelength).

Similarly, let the infrared radiance be $N_I(\xi)$, where it is assumed that N_I is a function of the satellite angle ξ only. Then $N_I(\xi)$ can be written as

$$N_I(\xi) = m[\epsilon(\xi)B_c + (1 - \epsilon(\xi))B_g] + (1 - m)B_g \quad (3)$$

$$= B_g - m\epsilon(\xi)(B_g - B_c), \quad (4)$$

where B_g and B_c are the effective blackbody radiances (for the spectral range of the IR radiometer) for the surface and cloud temperatures T_g and T_c respectively and $\epsilon(\xi)$ is the emittance of the cloud along a slant path at ξ to the vertical. The radiance B_g includes continuum absorption and emission of radiation by water vapour between the cloud layer and the surface but the effects of water vapour between the cloud and space are neglected.

The effective brightness temperature T_e for the radiometer FOV is related to $N_I(\xi)$ through an effective blackbody radiance curve for the radiometer spectral band.

It can be seen that for given cloud and surface temperatures, $N_I(\xi)$ varies with cloud amount m, together with the cloud and surface albedoes.

It is evident that to obtain the bispectral relationship between α_e and α' and T_e, for given values of m, B_c, B_g and α_g, a relation is required between $\alpha(\theta)$ and $\epsilon(\xi)$. These two quantities are linked through the basic scattering and absorption properties of the cloud particles. Thus $\alpha(\theta)$ can be related to visible cloud optical depth δ_c theoretically, if the single scattering properties of the cloud particles are known. This has been done by Hansen (1969) for spheres, to simulate water clouds and by Liou (1973) for ice cylinders to simulate ice clouds. These calculations were done for non-absorbing particles in the visible region which is valid below 0.7 μm wavelength. Similarly, for a given spectral band and particle size distribution and phase and infrared cloud optical depth can be calculated and then related to the visible optical depth by a factor of g (say),

$$g = \delta_c/\delta_a, \quad (5)$$

where δ_a is the absorption optical depth (in the 10–12 μm wavelength interval for this study). The absorption optical depth is used because infrared scattering is neglected. A correction for scattering for high clouds is considered later in Section 2e.

The dependence of g on particle size was given by Platt (1979) (α was used instead of g in that article)

for both water spheres and ice cylinders based on the theory calculations by G. L. Stephens (private communication, 1978). For ice cylinders, with particles larger than 10 μm radius, g had a value of 2. For water clouds and for boundary layer clouds in particular, the cloud drop radius varies in the range of 1 to 10 μm (e.g., Paltridge and Platt, 1976). Over this range, the average value of g was about 2.5.

The absorption emittance $\epsilon(\xi)$ is then given by (Platt and Stephens, 1980)

$$\epsilon(\xi) = [1 - \exp(-\delta_a \sec\xi)] \quad (6a)$$

$$= [1 - \exp(-\delta_c g^{-1} \sec\xi)]. \quad (6b)$$

Curves of $\alpha(\theta)$ versus $\epsilon(\xi)$ are shown in Figs. 1a and 1b for water clouds and ice clouds respectively and for $\xi = 0$. The curves are based on Hansen's (1969) computations of $\alpha(\theta)$ versus δ_c for water clouds and similar computations by Liou (1973) for ice cylinders. The observations of Platt *et al.* (1980) and Paltridge and Platt (1981) indicate that the ice cylinder model gives a reasonably accurate simulation of ice cloud albedo.

In order to illustrate the bispectral properties of a single cloud layer, it is convenient to consider two limiting cases.

First, consider an unbroken extended cloud layer ($m = 1$), but with an optical depth which varies from one FOV to another. Then Eqs. (2) and (4) reduce to

$$\alpha_e = \alpha(\theta) + \frac{(1 - \alpha')^2 \alpha_g}{1 - \alpha' \alpha_g}, \quad (7)$$

$$N_I(\epsilon) = B_g - \epsilon(\xi)(B_g - B_c); \quad (8)$$

also

$$T_e = f(N_I(\epsilon)). \quad (9)$$

The bispectral curves for single cloud layers at two different altitudes are shown as curve 1 in Figs. 2a and 2b. The cloud temperatures and phases and the underlying surface properties and angles ξ and θ are shown in Table 1.

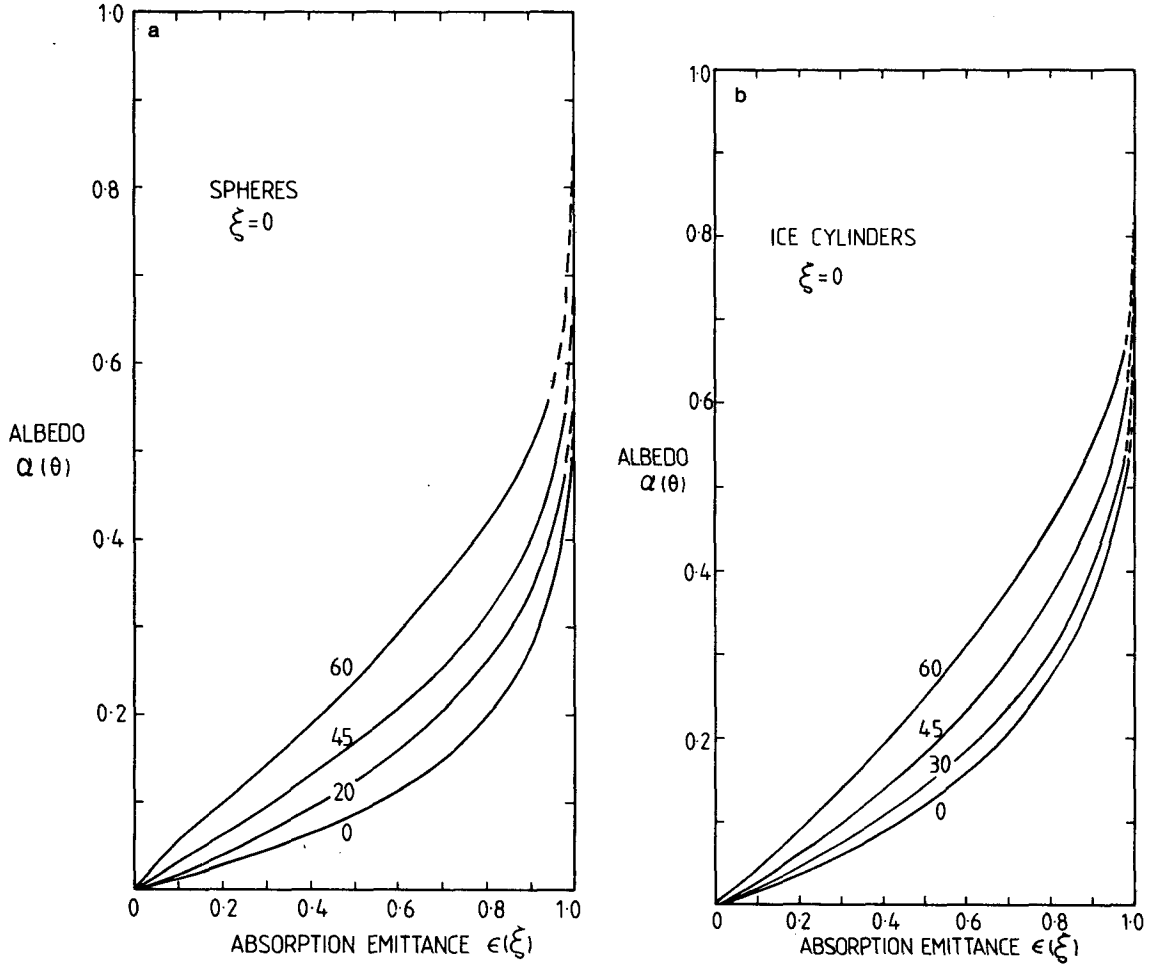

FIG. 1. Curves of visible albedo $\alpha(\theta)$ versus infrared absorption emittance $\epsilon(\xi)$ for (a) model water clouds (spheres) for $\xi = 0$ and for various solar zenith angles (after Hansen, 1969) and (b) model ice cylinder cloud (After Liou, 1973).

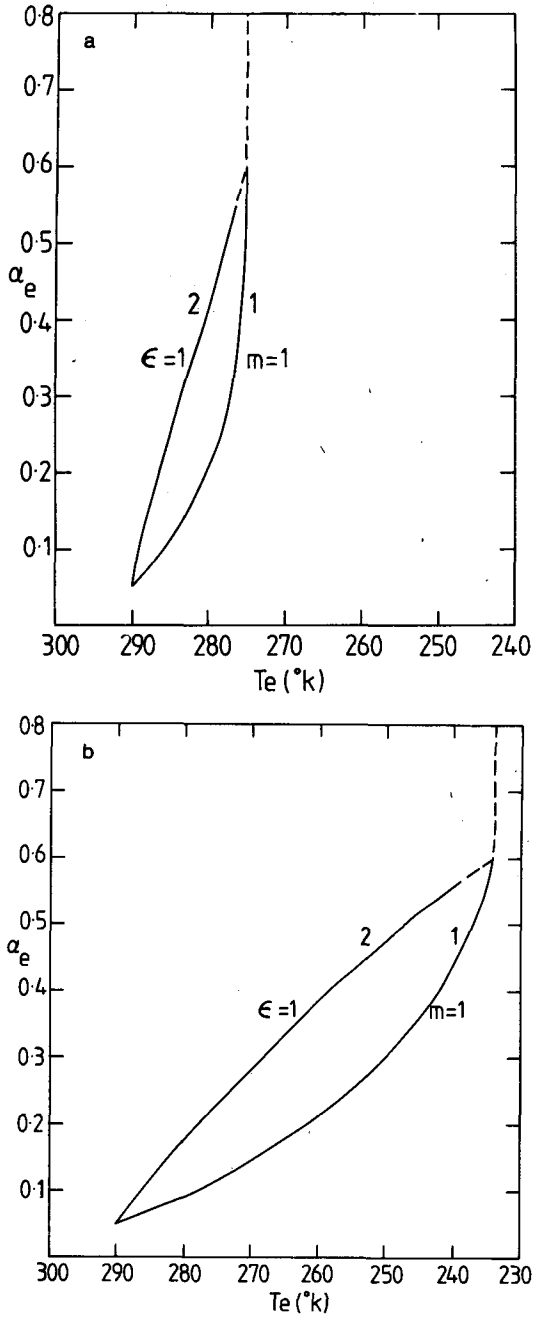

FIG. 2. Bispectral curves of albedo α_e versus brightness temperature T_e for (a) low cloud layer and (b) a high cloud. Line 1 unbroken layer with variable optical depth; line 2 broken layer of cloud of constant optical depth ($\epsilon \approx 1$).

The procedure used to calculate the curves was to choose a visible optical depth δ_c, calculate $\epsilon(\xi)$ from Eqs. (5) and (6) and T_e from Eqs. (8) and (9) using a calibration curve of T_e versus N_I for the 10–12 μm region; then obtain $\alpha(\theta)$ from either Figs. 1a or 1b, depending on the phase of the cloud, and calculate α_e from Eq. (7). Values of the diffuse albedo α', for various values of ϵ, are given in Table 2. Values were

TABLE 1. Parameters used in single-layer calculations.

	Boundary layer cloud	High cloud
T_c (K)	275	233
T_g (K)	290	290
α_g	0.05	0.05
Phase	Water	Ice
θ (deg)	30	30
ξ (deg)	0	0
$\alpha(\delta_c, \theta)$	0.6	0.6
g	2.5	2.0

calculated using the method given in Platt *et al.* (1980).

The curves illustrate how α_e and T_e (i.e., the visible and infrared radiances) change as the cloud optical depth is varied. As $\epsilon(\xi)$ increases, Eq. (8) shows that the radiance $N_I(\xi)$ decreases linearly with $\epsilon(\xi)$. When $\epsilon(\xi) = 1$, then $N_I(\xi) = B_c$. On the other hand, as $\epsilon(\xi)$ increases, α_c increases, but this increase is very non-linear, reflecting the rates of change of $\alpha(\theta)$ with $\epsilon(\xi)$ shown in Fig. 1. The change in T_e with N_I is also non-linear such that it reduces the curvature in the $\alpha_e - T_e$ curve, but not to any great extent. The net result is that α_e increases only slowly with decreasing T_e when $\epsilon(\xi)$ is small, but very rapidly with decreasing T_e when $\epsilon(\xi)$ approaches unity. The bispectral curve thus approximates a J in shape.

The second case which we consider is one where the cloud is uniformly dense, with an emittance approaching unity, but the cloud amount m varies from one radiometer FOV to the next. It is assumed that the cloud albedo is uniform and equal to $\alpha(\delta_c)$, where the optical depth δ_c is large. Eqs. (2) and (4) then become

$$\alpha_e = m\alpha(\delta_c, \theta) + \frac{(1 - m\alpha'(\delta_c))^2\alpha_g}{1 - \alpha'(\delta_c)\alpha_g}, \qquad (10)$$

$$N_I(\xi) = mB_c + (1 - m)B_g. \qquad (11)$$

The albedo $\alpha'(\delta_c)$ is the diffuse albedo of the cloud for an optical depth δ_c.

The albedo α_e will increase as the fraction m increases, and this increase is found to be almost linear, particularly for small α_g. Similarly, $N_I(\xi)$ will also increase linearly with m. However the non-linear dependence of N_I on T_e is such that it causes the re-

TABLE 2. Diffuse albedo α' for water sphere and ice cylinder cloud models.

ϵ	Sphere	Cylinder
0.2	0.078	0.085
0.4	0.16	0.18
0.6	0.25	0.29
0.8	0.35	0.40
0.9	0.42	0.49
0.95	0.48	0.58

sultant spectral curves, shown as 2 in Figs. 2a and 2b, to be slightly curved, and in the opposite sense to curves 1. The value of $\alpha(\delta_c, \theta)$ has been assumed arbitrarily to be 0.6.

The variations of α_e and T_e in curves 2 are brought about by a change in *cloud amount m,* whereas the variations in curves 1 are due to a change in *cloud optical depth.* Thus, these two clear-cut cases should be distinguished in principle by visual inspection of a bispectral curve. For real clouds, the sensitivity of this method will of course depend upon both the resolution in the temperature and albedo values and the natural spread in values being significantly less than the separation of curves 1 and 2.

If m and $\alpha(\theta)$ (that is, δ_c) both vary from one FOV to the next, then, providing $\alpha(\theta)$ is less than 0.6, the corresponding values of α_e and T_e will define points lying within the space bounded by curves 1 and 2 of Fig. 2. Although the quantitative evaluation of m and $\epsilon(\xi)$ is not the central thesis of this paper, it is apparent that for a single cloud layer whose radiances can be categorized by Eqs. (2) and (4), together with Eqs. (5) and (6), then m and $\epsilon(\xi)$ can be solved uniquely. Methods of calculating m and $\epsilon(\xi)$ are obviously vital for the ISCCP and will be addressed in a future paper.

b. *Variation of α_e with solar zenith angle*

The above discussion has assumed a fixed solar zenith angle θ equal to 30°. If θ varies, then the dependence of $\alpha(\theta)$ on $\epsilon(\xi)$ will vary and this will affect the shapes of curves 1 (but not curves 2). This variation can be obtained theoretically, as shown in Fig. 1. The effect on the bispectral curve 1 of Fig. 2b for a single unbroken layer ($m = 1$) and variable optical depth is shown in Fig. 3. Comparing these curves with curve 1 in Fig. 2b it is evident that the curvature becomes more pronounced for small solar zenith angles. Thus, discrimination of changes in cloud amount from changes in optical depth should become more sensitive at small solar zenith angles.

c. *Variation of T_e with satellite viewing angle*

The emittance of the cloud $\epsilon(\xi)$ will change with satellite nadir angle ξ according to Eq. 6. For a given cloud optical depth δ_a, the observed brightness temperature T_e will thus also vary with ξ. Again this will only affect the shapes of curves 1. This effect is shown in Fig. 4 for the same cloud (curve 1) as shown in Figs. 2b and 3. The curvature increases with increasing nadir angles, and thus the discrimination of cloud amount from optical depth will improve with increasing ξ.

Variations of the shapes of the bispectral curves 1 with θ and ξ do not change the general result of the present model that cases of variable m can be distinguished in principle from cases of variable ϵ. However, the sensitivity of the method will change as indicated. Whether the present model is adequate to describe radiance from actual cloud fields and whether the scatter in radiances due to various factors is small enough to allow the above discrimination can only be decided by comparison of the method with actual satellite data.

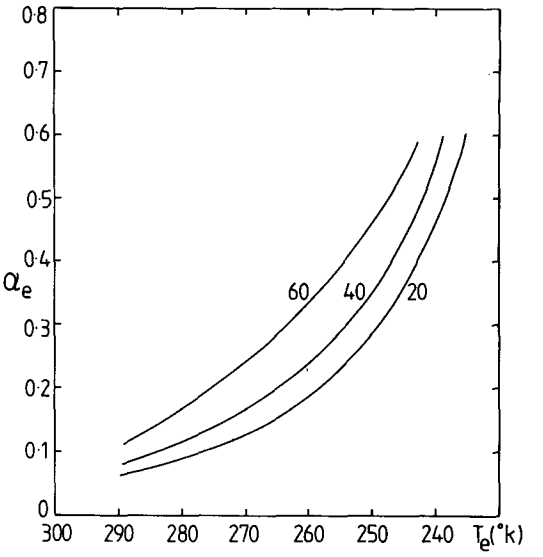

FIG. 3. Change in bispectral curves, for an unbroken layer and variable optical depth, with solar zenith angle θ (deg).

d. *Multiple cloud layers*

Single layers of cloud are not uncommon. For instance, the large areas of marine stratocumulus which

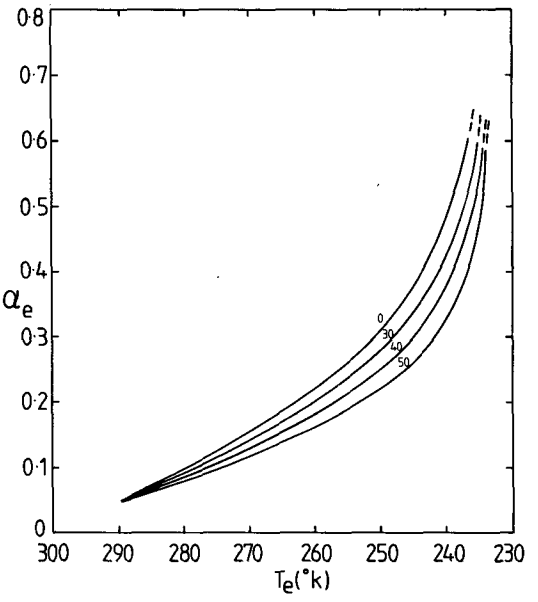

FIG. 4. Change in bispectral curves, for an unbroken layer and variable optical depth, with satellite nadir angle ξ (deg).

are prevalent in some regions of the globe, or the extensive areas of cirrus which exist on their own. However, multiple cloud layers are also common, for instance, in frontal situations, or where high cirrus cloud overlies boundary layer convective cloud. The equations for a multiple cloud layer situation are analogous to the single-layer situation.

The equations for α_e and $N_I(\xi)$ for a two-layer situation are

$$\alpha_e = n\alpha_2(\theta) + \frac{(1 - n\alpha_2')^2\alpha_{mg}}{1 - n\alpha_2'\alpha_{mg}}, \quad (12)$$

where

$$\alpha_{mg} = m\alpha_1(\theta) + \frac{(1 - m\alpha_1')^2\alpha_g}{1 - m\alpha_1'\alpha_g}, \quad (13)$$

$$B_e = B_g - n\epsilon_2(\xi)(B_g - B_2) - m\epsilon_1(\xi)(1 - n\epsilon_2(\xi))(B_g - B_1). \quad (14)$$

Here, n and m are the cloud fractions for the upper and lower layer respectively and B_2 and B_1 are the corresponding effective blackbody radiances. It is assumed that the cloud regions in the two layers are dispersed quite randomly. The albedo α_{mg} is the effective albedo of the lower layer and the ground when viewed from the upper layer. The additional assumption made in Eq. (13) is that the albedo of the lower cloud layer to the solar radiation transmitted by the layer is equal to the albedo to direct radiation. This will be true for incident solar radiation passing through gaps in the top layer, but not for radiation which is transmitted by the cloud in the top layer. However, the error in this treatment is estimated to be small.

The bispectral curves in this case are functions of four independent variables m, n, ϵ_2 and ϵ_1, resulting in a large family of curves. To illustrate the shapes of these curves, the equations are simplified to represent two situations which occur in the real atmosphere. First, consider two cloud layers which both have high optical depths, but which are likely to be broken; for instance, cirrocumulus overriding altocumulus. It is assumed then that $\epsilon_1(\xi) = \epsilon_2(\xi) = 1$ and again that $\alpha_2 = \alpha_1 = 0.6$. Other parameters used are listed in Table 3. The resultant family of curves for different values of n and m are shown in Fig. 5. If the two cloud layers contain randomly spaced clouds of variable fractional amount, then there will no longer be a single curve, but a collection of points bounded by the curves shown. In this case, each point in the space bounded by the outer curve gives a unique value of n and m. Of course, in general, α_2 will not be equal to α_1, and different shaped curves will be obtained. One feature of the curves is the high albedo when m and n both approach unity. This is caused by the multiple reflections between the two cloud layers.

TABLE 3. Parameters used in double-layer calculations.

	Bottom cloud layer	Top cloud layer
T_c (K)	260	233
T_g (K)	290	290
α_g	0.05	0.05
Phase	Ice	Ice
	30°	30°
	0°	0°

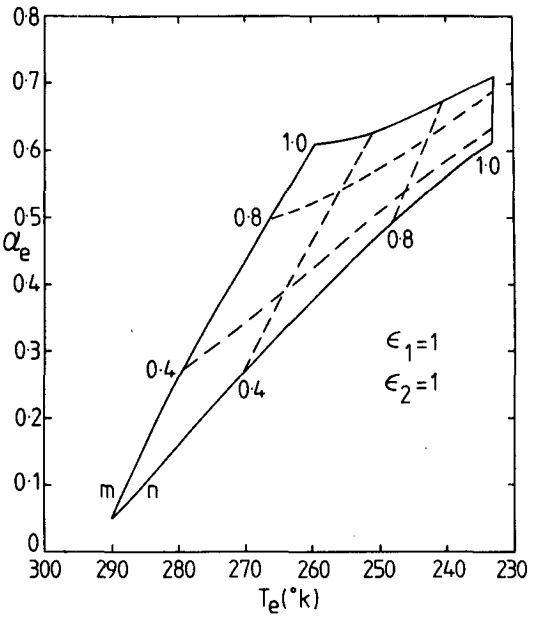

FIG. 5. Family of bispectral curves for two overlapping cloud layers. Both cloud layers are broken but cloudy areas have uniform optical depth.

The second case we consider is an unbroken high layer (cirrostratus) overlying a lower layer of cumulus or altocumulus. Here we assume that $n = 1$ and ϵ_2 is variable but $\epsilon_1 = 1$ and m is variable. The resultant family of curves is shown in Fig. 6. For a high cloud which contains regions of widely varying optical depth and a lower cloud with variable fractional amount, points will again lie in the space bounded by the curves, and each point will define a unique value of ϵ_2 and m. When ϵ_2 approaches unity, the maximum value of α_e will depend on the maximum optical depth of the upper cloud. Again, the two cloud layers interact to give enhanced values of α_e through multiple scattering particularly when m and ϵ_2 together approach unity.

Whether various types of overlapping clouds in the real atmosphere give identifiable signatures such as those of Figs. 5 and 6 is something which is still to be established. However the above cases once again give a physical basis for the determination of the cloud amounts and optical depths, although it is not the purpose of this paper to go into such determinations.

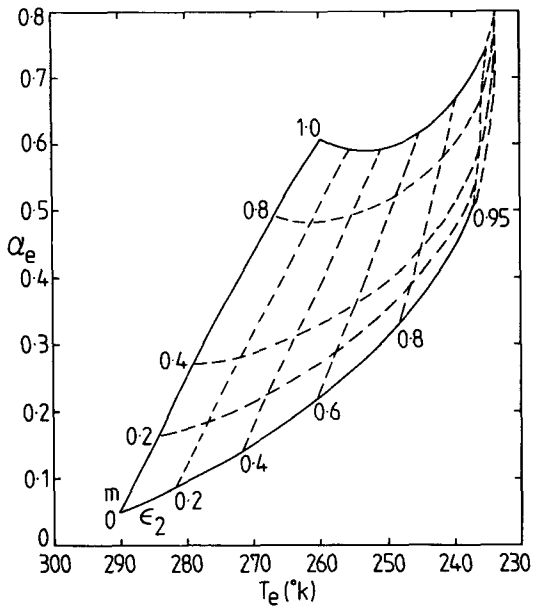

FIG. 6. Family of bispectral curves for two overlapping cloud layers. Top layer is unbroken with cloud of variable optical depth. Bottom layer is broken but with cloud of uniform optical depth.

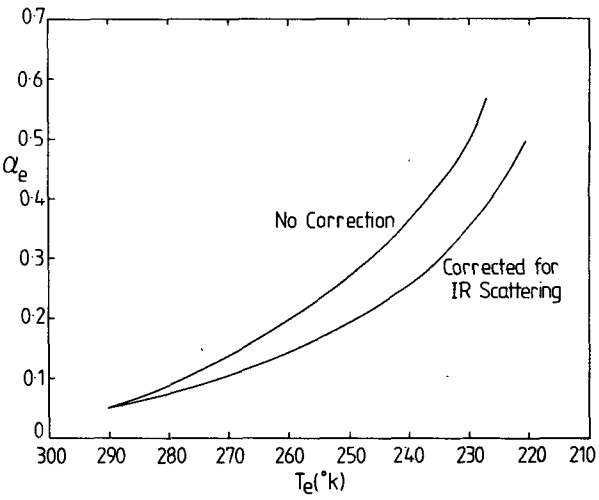

FIG. 7. Change in the bispectral curve of a high cloud layer when infrared scattering and deep cloud effects are taken into account. Cloud layer is unbroken with variable optical depth.

e. Single layers of deep cloud and infrared scattering effects

The treatment so far has considered relatively thin, isothermal cloud layers, and has neglected infrared scattering effects. Many cloud systems associated with disturbed weather consist of layers many kilometers deep. These layers are obviously not isothermal and the total infrared radiance at the cloud top is the integrated effect from many layers at different temperatures. Under these conditions, the effective radiating temperatures will depend on both the temperature profile and the cloud optical depth. Infrared scattering is also important, particularly for high clouds, because some upwelling radiation from the earth's surface is scattered back by the cloud without being transmitted and similarly the emission from the cloud top is effectively reduced. The above two effects together decrease the observed brightness temperature below the value corresponding to mid-cloud temperature, that is, they increase the effective cloud emittance ϵ. This change in emittance has been worked out by Platt and Stephens (1980) who give values for effective emittances which can be applied directly to equations such as Eq. (4) of this paper.

An example of the change in brightness temperature T_e for a given albedo α_e due to the above effects is shown in Fig. 7 for a cloud two kilometres deep. For the isothermal case, the cloud temperature was taken as 225 K, and the cloud was assumed to be unbroken, with a variable optical depth. The change in the effective radiating temperature is very considerable. At $\epsilon = 0.95$, it amounts to nearly 10 K. The effective emittances of the cloud used in the calculation are shown in Table 4.

One potential advantage of this effect is that for high clouds and highly absorbing deep clouds the observed brightness temperature is shifted towards the cloud top temperature, which is one of the temperatures required for the ISCCP. It is obvious that in any method which seeks to obtain the cloud top temperature full cognizance of scattering effects must be taken.

f. Other effects—"finite" clouds and anisotropy of solar albedo

This study has attempted to make the model as physically realistic as possible. But as mentioned previously, it doesn't necessarily follow that the model is correct for real clouds in the atmosphere. For instance, it is known from observation that cloud top heights within a layer can vary, leading to variations in T_c. But a potentially greater problem is that the albedo–emittance relationships of Fig. 1 have been computed for an *infinite layer,* whereas real clouds can have *finite* dimensions with depths which can be greater than their widths. McKee and Cox (1974) were the first to show that the radiances out of the

TABLE 4. Effective emittances used for curve 2 in Fig. 7.

Emittance ϵ	Effective emittance ϵ'
0.2	0.29
0.4	0.56
0.6	0.77
0.8	0.94
0.9	1.0
0.95	1.04

tops of 'finite' clouds are considerably lower than for an extended cloud of similar optical depth, because radiation 'leaks' from the sides. Thus finite clouds have the capacity for depressing the albedo. A preliminary calculation indicates that the effects of finite clouds could themselves explain some of the J-shape of the bispectral curves. Obviously, such effects will depend on the angles θ, ϕ and ξ, and the situation is complex. Because of a dearth of radiance data for various conditions, no attempt is made here to examine the effects of finite cloud on bispectral curves. However, the analysis here carries with it the caveat that such effects do exist.

Another important factor which has not been considered in this study is the pronounced anisotropy of the solar albedo of clouds. This effect causes the cloud radiance to vary, for a given zenith angle θ, with the azimuth angle ϕ between the solar direction and the satellite direction. Information on this effect is very sparse and both theoretical computations and observations are urgently needed.

3. Comparison of predicted bispectral curves with observational data

Since the original work of Reynolds and Vonder Haar (1977) very little observational work has been published. Coakley and Bretherton (1981 and unpublished) gave some examples of bispectral curves for boundary layer stratus and Desbois *et al.* (1982) gave a few examples of bispectral curves. Their results will be discussed presently.

Platt (1981) presented bispectral data in the form of two-dimensional histograms, and the results of this study are now considered. The histograms were formed by summing the total number of pixels in a given surface area which had IR brightness temperature values and visible albedo values lying between specified limits. Thus the histograms gave, in effect, bispectral curves which had been smoothed out over the temperature and albedo intervals. Data were obtained from the VISSR radiometer of the GMS-1 Japanese Geostationary Satellite. Two-dimensional histograms were constructed with temperature intervals of 5 K and visible albedo intervals of 0.025. The histograms were subsequently contoured and the contours smoothed.

In the study of Platt (1981), areas of cloud which represented various synoptic systems were chosen by visual inspection of hard copy satellite pictures. Regions approximately 500 × 500 km^2 in area were selected, corresponding to about 40 000 pairs of IR and visible data.

Figs. 8a–d give some examples of 2-D histograms obtained by Platt (1981). Common features of the histograms are maxima in values at various points in the histogram. The corresponding IR and visible values can often be identified at either surface or cloud top quantities. Because of the relatively coarse resolution in temperature, some of the bispectral structure is lost, particularly for low clouds, where the temperature difference between the cloud and surface is small.

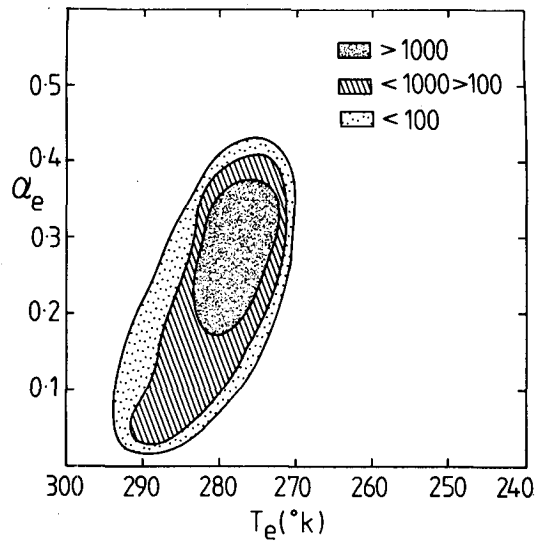

FIG. 8a. A two-dimensional bispectral histogram for an area of boundary layer cloud over sea. Data from GMS-1 0000 GMT 10 April 1980, mean latitude (ψ) 37.5°S, mean longitude (ϕ) 157.5°E. Local time t = 1030 LT, $\mu(\cos\theta)$ = 0.814. Area A = 500 × 500 km^2. The legend differentiates the number of counts for each pair of albedo–temperature values. Contours have been smoothed.

Fig. 8a shows a histogram indicating a cloud top temperature of from 275 to 280 K. The shape of the histogram approximates that of Fig. 2a although the coarseness of the histogram intervals would appear to wash out any chance of discriminating between cloud amount and optical depth. However, a J-shape is still discernible. The lowest observed albedo of

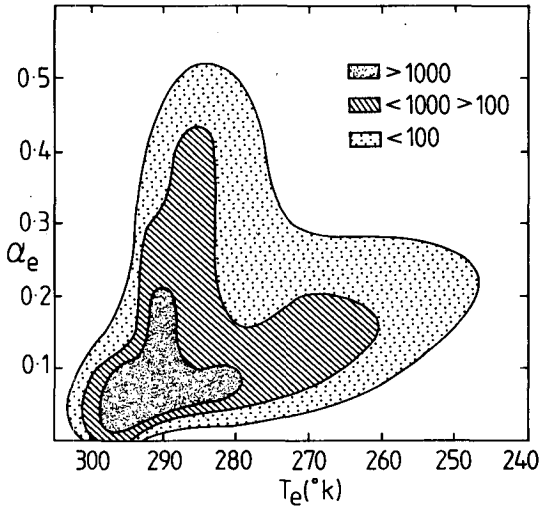

FIG. 8b. As in Fig. 8a, for boundary layer cloud over sea (trade-wind cumulus and some high cloud) 0000 GMT 13 April 1980, ψ = 17.5°S, ϕ = 157.5°E, t = 1030 LT, μ = 0.919, A = 500 × 500 km^2.

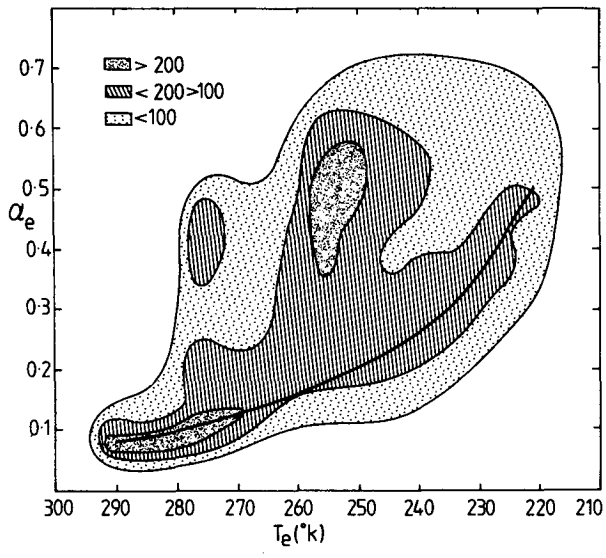

FIG. 8c. As in Fig. 8a, but for multiple cloud layers over sea (frontal cloud), 0600 GMT 9 January 1980, ψ = 35°S, ϕ = 125°E, t = 1420 LT, μ = 0.837, A = 500 × 500 km^2. Wide full line: see text.

about 0.05 is typical for a sea surface, indicating that the histogram is for a cloud layer situated over the sea and with a sea-surface temperature of 290 K. There appears to be no other cloud layer at a lower temperature. The *maximum* albedo of 0.4 would indicate, assuming an isotropically reflecting cloud for a zenith angle of 35.5° and using Fig. 1a, a maximum cloud absorption infrared optical depth of 3.5 ($\epsilon \sim 0.97$) and thus a visible optical depth δ_c of about 8.5 (g = 2.5). The hard copy visible and infrared images taken by satellite as in Platt (1981) give some verification that the cloud analysed was indeed boundary layer cloud over the sea.

Fig. 8b again points to boundary layer cloud over the sea, but with an additional cloud feature appearing. The sea surface temperature is about 300 K and the boundary layer cloud top has a temperature of about 285 K. The additional "tongue" would possibly indicate semitransparent high cloud. The area studied, off the coast of northeastern Australia, is one where boundary layer tradewind cumulus and stratocumulus are typically prevalent and flecks of high cloud are apparent in the hard copy image.

Fig. 8c reveals a complex situation with two cloud tops having temperatures of 275 and 253 K, respectively, as indicated by the maxima in the contours, and a sea surface temperature of 290 K. In the upper cloud deck the maximum albedo of 0.6 points to quite a high optical depth for this cloud. There is also apparently a semi-transparent high cloud layer which, over at least part of the region considered, does not overlap the other cloud decks. For this latter cloud a more quantitative comparison with predicted bispectral curves has been attempted. It was assumed that the cloud layer was unbroken with a variable optical depth. The resultant curve is shown superimposed on the histogram in Fig. 8c; parameters used to obtain the fit are given in Table 5. Effects of infrared scattering were taken into account. If the area of the histogram encompassed by the fitted curve does represent semitransparent cloud, then the fit is very good. The hard copy output (Platt, 1981) indicated that the region analysed was covered by a broad band of pre-frontal cloud. The layering in such a cloud is likely to be complex, and the conclusions drawn from the histogram seem to be realistic. One conclusion drawn from the shape of the histogram, when this is compared with Figs. 2a and 2b, was that not much of the cloud layer was broken and most variations were due to changes in optical depth. This could not,

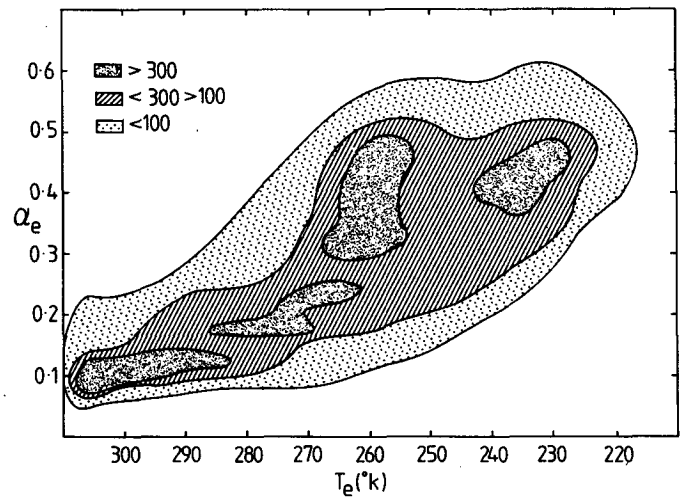

FIG. 8d. As in Fig. 8a, but for multiple cloud layers over land. 0600 GMT 11 April 1980, ψ = 27.5°S, ϕ = 122.5°E, t = 1417 LT, μ = 0.810, A = 500 × 500 km^2.

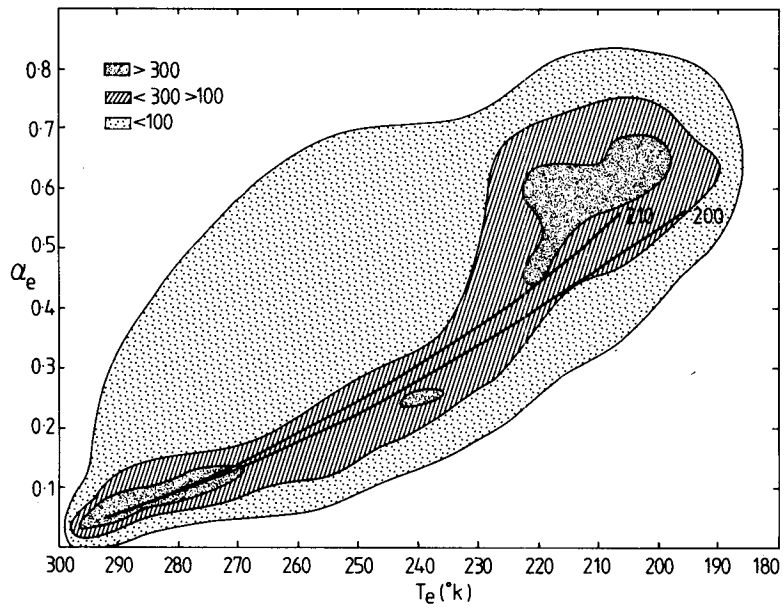

FIG. 8e. As in Fig. 8a, but for tropical clouds. 0600 GMT 11 April 1980, ψ = 2.5°N, ϕ = 137.5°E, t = 1510 LT, μ = 0.66, A = 500 × 500 km^2. Wide full lines: see text.

of course, be verified. Fig. 8d shows another complex situation, with cloud top temperatures of 235 and 260 K. This histogram is included as a possible example of completely overlapping cloud decks, the bispectral shape approximating that of Fig. 6.

Fig. 8e is a histogram of what is obviously yet another complex situation. Comparing Figs. 2b and 8e, that part of the histogram at temperatures greater than 230 K, would certainly appear to be due to a deck of semitransparent cloud. Two predicted bispectral curves for a single layer of semitransparent cloud with cloud top temperatures of 200 and 210 K, respectively, are also shown. Parameters used to calculate these curves are given in Table 5. Infrared scattering effects have again been included. The fit of these curves along the narrow section of the curve is quite good.

The large area of cloud represented by that part of the histogram between 200 and 220 K and with an albedo greater than 0.5 is interpreted as deep convective cloud under and around the cirrus deck. It is interesting that the shape of the histogram in this region, which exhibits a slow increase in albedo as T_e decreases, approximates that part of the bispectral curve of Fig. 5 where n is variable (i.e., dense high cloud of variable amounts) and m is near unity (i.e., widespread convective cloud). These conclusions do not disagree with the hard copy image for this occasion (Platt, 1981) which shows what is apparently a large cloud cluster situated in tropical waters with extensive cirrus outflow. It is apparent that much of the cirrus cloud did not overlap the convective cloud.

TABLE 5. Parameters used to fit curves to histograms.

	Fig. 8c	Fig. 8e
α_g	0.07	0.05
T_g (K)	290	292
T_c (K)	225	200, 210
θ (deg)	33	49
ξ (deg)	35	−2.5

In all of the above cases there is no ground truth to aid in verifying the conclusions regarding cloud types, and it is only possible to make some judgement of cloud type by appeal to the patterns, locations and relation to the synoptic situation of the cloud fields revealed in the hard copy images.

Of the other authors mentioned previously, Coakley and Bretherton (unpublished) have shown bispectral, high resolution curves which exhibit surprisingly well-defined J-shapes, even for boundary layer clouds. Unfortunately, no ground truth existed for this data. Coakley and Bretherton (1982) give one bispectral curve, which does exhibit a J-shape, but they dismiss the variations in albedo as due to holes or irregularities in the cloud, whereas the present study indicates that the variations were much more likely to be due to variations, at least in part, of cloud optical depth.

The bispectral curve for a high cloud given by Desbois *et al.* (1982) looks very similar to the curves 1 in Figs. 2a and 2b representing semi-transparent unbroken cloud.

4. Discussion

It is clear from this study that, at least theoretically, information on cloud cover and cloud optical depth

can be recovered separately from geostationary satellite bispectral data. Whether the method works in practice even for a single cloud layer depends, apart from any deficiencies of the model, on the spatial resolution of the satellite data and its accuracy. The good quantitative comparisons between predicted and observed bispectral curves for semitransparent high clouds which are shown in Figs. 8c and 8e (with the caveat that it really is high cloud which is being observed) lend credence to the model developed in the present study, at least for this type of cloud. The problem of identification of thin cirrus is very prominent in the formulation of plans for the ISCCP. It is obviously important to check the method for high cloud and this will be attempted shortly at Aspendale by comparing satellite observations with observations of cloud height, depth and optical depth obtained with LIDAR.

In order to test the model more fully, particularly for boundary layer stratus and convective clouds, and frontal clouds, effects on the radiance of finite clouds and the anisotropy of cloud reflection must be fully incorporated in the model. This can be done to a certain extent by theoretical methods, but it will also require airborne studies of the radiances over real cloud fields, with simultaneous satellite data, together with careful documentation of cloud type, optical depth and pattern.

Before the method can be used operationally for the ISCCP it is also necessary to develop and automate methods for actually extracting cloud data from the bispectral information. The methods could either be pattern recognition techniques or full numerical inversion methods. This development should go hand-in-hand with the development and refinement of the bispectral model itself.

A possible method of making the model even more sophisticated and thus obtaining more detailed cloud information is to retain the coherence between *three or more* sets of satellite data. Coakley and Bretherton (1982), for instance, describe a novel method for obtaining detailed information from IR data by a spatial coherence technique. In their method, the standard deviation of the radiance over a small area is plotted against the mean radiance. For a single cloud layer over the sea, the points then follow an arch-shape with the 'feet' of the arches representing clear radiances or unbroken cloud and the large standard deviation in between representing broken cloud decks. Although the method has the advantage of applicability for both day and night, it yields no information on optical depth. It is clear from Fig. 1 that the visible albedo provides the most sensitive measure of optical depth. This points to the potential usefulness of combining the bispectral and spatial coherence methods to give a three-dimensional representation. This additional dimension might provide some sort of discrimination between finite clouds (variable ϵ and α and high standard deviation) and unbroken clouds of variable optical depth (variable ϵ and α but lower standard deviation).

This article has given a physical basis to bispectral curves with the hope of being able to deduce detailed cloud information from the standard visible and IR channels of the geostationary satellites. Although the effects of finite or irregular clouds may be considerable, the existence of distinctive bispectral signatures as shown in Figs. 8a to 8e, together with the knowledge accumulated over many years through visual observations that clouds tend to be arranged in characteristic patterns or layers, makes such a hope justifiable.

Even if suitable operational algorithms based on the arguments advanced here are not available for several years it is important that the *coherence* of the visible and IR data in the ISCCP should be *maintained* to make such detailed analyses possible eventually.

REFERENCES

Coakley, J. A., Jr., and F. P. Bretherton, 1982: Cloud cover from high-resolution scanner data: detecting and allowing for partially filled fields of view. *J. Geophys. Res.*, **87**, 4917–4932.

Desbois, M., G. Seze and G. Szejwach, 1982: Automatic classification of clouds on METEOSAT imagery: Application to high-level clouds. *J. Appl. Meteor.*, **21**, 401–412.

Hansen, J. E., 1969: Exact and approximate solutions for multiple scattering by cloudy and hazy planetary atmospheres. *J. Atmos. Sci.*, **26**, 478–487.

Liou, K. N., 1973: Transfer of solar irradiance through cirrus cloud layers. *J. Geophys. Res.*, **78**, 1409–1418.

McKee, T. B., and S. K. Cox, 1974: Scattering of visible radiation by finite clouds. *J. Atmos. Sci.*, **31**, 2182–2188.

Paltridge, G. W., and C. M. R. Platt, 1976: *Radiative Processes in Meteorology and Climatology.* Elsevier, 318 pp.

——, and ——, 1981: Aircraft measurements of solar and infrared radiation and the microphysics of cirrus cloud. *Quart. J. Roy. Meteor. Soc.*, **107**, 367–380.

Platt, C. M. R., 1979: Remote sounding of high clouds. I: Calculation of visible and infrared optical properties from lidar and radiometer measurements. *J. Appl. Meteor.*, **18**, 1130–1143.

——, 1981: Two-dimensional histograms of GMS-1 satellite visible albedo and infrared temperature for selected cloud systems. CSIRO Div. Atmos. Phys., Tech. Paper No. 40, 43 pp.

——, and G. L. Stephens, 1980: Interpretation of remotely sensed high cloud emittances. *J. Atmos. Sci.*, **37**, 2314–1322.

——, D. W. Reynolds and N. L. Abshire, 1980: Satellite and lidar observations of the albedo, emittance and optical depth of cirrus compared to model calculations. *Mon. Wea. Rev.*, **108**, 195–204.

Reynolds, D. W., and T. H. Vonder Haar, 1977: A bispectral method for cloud parameter determination. *Mon. Wea. Rev.*, **105**, 447–457.

Stephens, G. L., 1978: Radiation profiles in extended water clouds. I: Theory. *J. Atmos. Sci.*, **35**, 2111–2122.

——, 1980: Radiative transfer on a linear lattice: Application to anisotropic ice crystal clouds. *J. Atmos. Sci.*, **37**, 2095–2104.

——, G. W. Paltridge and C. M. R. Platt, 1978: Radiation profiles in extended water clouds. III: Observations. *J. Atmos. Sci.*, **35**, 2133–2141.